How the universe got its spots

Janna Levin,[1] Evan Scannapieco,[1] Giancarlo de Gasperis,[1] Joseph Silk,[1] and John D. Barrow[2]

[1]*Center for Particle Astrophysics, UC Berkeley, Berkeley, California 94720-7304*

[2]*Astronomy Centre, University of Sussex, Brighton BN1 9QJ, United Kingdom*

The universe displays a three-dimensional pattern of hot and cold spots in the radiation remnant from the big bang. The global geometry of the universe can be revealed in the spatial distribution of these spots. In a topologically compact universe, distinctive patterns are especially prominent in spatial correlations of the radiation temperature. Whereas these patterns are usually washed out in statistical averages, we propose a scheme which uses the universe's spots to observe global geometry in a manner analogous to the use of multiple images of a gravitationally lensed quasar to study the geometry of the lens. To demonstrate how the geometry of space forms patterns, we develop a simple real-space approximation to estimate temperature correlations for any set of cosmological parameters and any global geometry. We present correlated spheres which clearly show topological pattern formation for compact flat universes as well as for the compact negatively curved space introduced by Weeks and another discovered by Best. These examples illustrate how future satellite-based observations of the microwave background can determine the full geometry of the universe. [S0556-2821(98)02124-9]

PACS number(s): 98.70.Vc, 98.80.Hw

From the zebra's stripes to the leopard's spots, the animal kingdom displays a diversity of coat patterns. Following the innovative ideas of Turing [1], mathematical biologists have posed and partly answered the question of how the leopard got its spots. The fluctuation of enzymes diffusing through the developing embryo can lead to the spatial pattern formation displayed by animal coats. Both the geometry and size of the animal exert a strong influence on differentiating patterns. For instance, the broad cylindrical shape of the leopard's body favors spots while the tapered tail induces stripes [2]. Remarkably, these diverse features can arise from the properties of simple solutions to second-order partial differential equations on the geometry and topology appropriate for animal limbs, tails, or bodies.[1]

Similarly, the global geometry of the universe can lead to distinctive pattern formation by the normal modes of vibration of the universe in the microwave sky, or even in the distribution of luminous galaxies. Unobscured by complicated evolutionary effects, the cosmic microwave background radiation (CMB) offers the best site to seek out patterning. When light last scattered off hot matter, small temperature fluctuations left birthmarks in the radiation. These hot and cold spots in the primordial radiation may be randomly distributed in an infinite universe, but if the universe possesses a compact topology then distinctive patterns

can be generated. Such topologically induced pattern formation has already been seen in simulated maps of the microwave sky [4,5].

The diffusive processes in biological systems actually simplify an animal's coat by singling out a particular mode and hence a particular pattern. By contrast, the universe contains many competing modes. While some simple large scale patterns are clearly evident in sky maps of the CMB temperature fluctuations [4,5], subtler patterns can be extracted from the observations. In particular, a correlation in temperature between pairs of points can scan the map and select out geometric features. Maps of correlations for different topologies populate the cosmic zoo of possibilities displayed in Secs. II and III.

CMB observations of the universe's hot and cold spots could be used as real-space pictures of geometry. With correlated maps we could observe topologically lensed images of the horizon at the time of last scattering. The number and pattern of lensed images of the horizon provide information about the geometry of the universe. A nice analogy is provided by observations of gravitationally lensed images of a quasar, the pattern and number of which reveal the geometry of the intervening lens. The universe's spots are too small in angular scale to have been detected by the Cosmic Background Explorer (COBE) but will be visible by the future satellite missions, MAP (Microwave Anisotropy Probe) and *Planck Surveyor*.

The fluctuations in the CMB can be described by decomposing the relative temperature fluctuations, $\delta T(\vec{x})/T = \int d^3\vec{k}\, \hat{\phi}_{\vec{k}} \psi_{\vec{k}}$, into a series of eigenmodes $\psi_{\vec{k}}$ each of which is a solution of Laplace's equation on the curved space of the universe, $(\nabla^2 + k^2)\psi_{\vec{k}} = 0$. The $\hat{\phi}_{\vec{k}}$ are primordially seeded amplitudes that on average define a spectrum of perturbations. Topology introduces boundary conditions which create a discretized set of wave vectors and complex relations between the $\hat{\phi}_{\vec{k}}$ [6]. This problem is tractable in the case of a

---

[1] For example, the two-dimensional Helmholtz equation

$$\nabla^2\phi + k^2\phi = 0,$$

with $(\mathbf{n}\cdot\nabla)\phi = 0$ on the boundary, has solutions which describe different geometric tessellations of alternating regions with $\phi > 0$ and $\phi < 0$, [3]. For example, an infinite line of one-dimensional stripes is described by the solutions $\phi = \cos kx$, with $k = n\pi$ for $n = \pm 1, \pm 2, ..$, whereas a solution $\phi = \frac{1}{2}[\cos kx + \cos ky]$, with $k = \pi$ or 2π describes a checker-board tessellation of space with alternating square spots, with $\phi > 0$ and $\phi < 0$, inclined at 45°.

flat universe but, for a compact hyperbolic space, the identi-fication rules lead to such intricate boundary conditions on the modes that they cannot be decomposed analytically [7]. This is a symptom of the chaotic hyperbolic flow of geodesics induced on these spaces. Microwave photons moving on compact hyperbolic manifolds thus demand more indirect methods of analysis. Cosmological observations favor a negative curvature and mathematics favors compact hyperbolic manifolds by providing an infinite number of candidates. The resistance encountered when subjecting these manifolds to conventional eigenmode treatments has sparked recent interest and produced several different approaches to the search for observational probes of the universe's global topology. Three strategies have emerged: a search for circles in the microwave sky [8], a search for spatial pattern formation [4,6], and a direct attack via the method of images [9]. All three approaches are necessarily related. We will see aspects of each emerge in our zoo of topological examples.

For reviews and other interesting papers on cosmic topology see Refs. [10–13].

I. TOPOLOGY AND THE ANGULAR CORRELATION FUNCTION

Compact spaces are specified by $\mathcal{M}=\mathbf{U}/\Gamma$ where $\mathbf{U}$ is the geometry of the infinite space before any compactifications are made. $\mathbf{U}$ is also known as the universal covering space. The generators $\{g_k\}$ of the group Γ provide the set of instructions for gluing together points in $\mathbf{U}$ in order to render the space finite and multiconnected. The elements of Γ form a discrete subgroup of the full isometry group of the covering space. A finite geometry has the same curvature as $\mathbf{U}$. The universal covering space is usually assumed to be a space of constant curvature, either the flat $\mathbf{E}^3$, the negatively curved $\mathbf{H}^3$, or the positively curved $\mathbf{S}^3$. The real universe does not have perfectly constant curvature over the entire manifold: its true topologies will then be a deformation of perfect polyhedra. The statement that the universe looks homogeneous and isotropic on average indicates that constant curvature will be a reasonable first assumption for finite manifolds which are comparable to or smaller than the Hubble scale of the visible universe. We limit ourselves to the subset of observationally viable manifolds with covering spaces of either the flat $\mathbf{E}^3$ or hyperbolic $\mathbf{H}^3$ variety.

In order to scan the sky for evidence of compact topology we use the correlation function for the temperature at two different points on the sky,

$$\left\langle \frac{\delta T(\hat{n})}{T}\frac{\delta T(\hat{n}')}{T}\right\rangle = C(\hat{n},\hat{n}'), \tag{1}$$

where $\hat{n}$ is a unit vector pointing from the Earth towards some location on the sky. The sphere of radius $\Delta\eta\hat{n}$ defines the surface from which we receive last-scattered photons. The size of the radius, $\Delta\eta$, is the conformal time between the time of last scattering and the present. The angular brackets denote an average over all possible realizations. In a simply connected cosmos, the assumption that the hot and cold spots are homogeneously and isotropically distributed ensures that
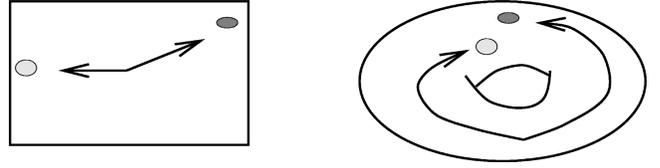
FIG. 1. Two points may appear to be far apart but if we identify opposite sides of the rectangle we see that the same points are actually close together on the compact torus.

the correlation function depends on only one parameter, namely the angle between the two points on the sky, that is $C(\hat{n},\hat{n}')=C(\theta)$ where $\cos\theta=\hat{n}\cdot\hat{n}'$. All of the information in an homogeneous and isotropic Gaussian field is contained in $C(\theta)$.

By contrast, topological identifications always break isotropy (with the exception of the projective space on $\mathbf{S}^3$) and most break homogeneity as well. The hypertorus on $\mathbf{E}^3$ is the only homogeneous compact space. Consequently, the correlation function, $C(\hat{n},\hat{n}')$, depends fully on $\hat{n}$ and $\hat{n}'$ and would require four dimensions for a full representation. Predicting $C(\hat{n},\hat{n}')$ is also more challenging on compact manifolds, particularly the compact hyperbolic spaces.

We will introduce a real-space approximation which captures all the important features necessary for examining global structure. Our approximation is based on two physical observations. First, two points which appear to be widely separated may actually be close together, as in Fig. 1: there is not a unique distance between points. Secondly, the correlation between two points is strongly peaked around short separations. While global topology drastically changes the large scale perturbations, it does not have a strong impact on scales much smaller than the size of the physical space. Therefore we expect the correlation function between nearby points to be well approximated by the correlation function of a simply connected universe.

Motivated by these two observations, we propose the following real space approximation to the angular correlation function: we take the correlation in temperature between two points on the surface of last scattering to be the correlation function in a simply connected universe given their minimum separation, that is,

$$C_{\mathcal{M}}(\hat{n},\hat{n}')\approx C^U[d_{\min}(\vec{x}(\hat{n}),\vec{x}'(\hat{n}'))], \tag{2}$$

where C^U is the correlation function on the universal cover, $\vec{x}(\hat{n})$ is the physical location of a point on the surface of last scattering, and $d_{\min}$ is the minimum distance between the two points in the topological space. To find the minimum distance we locate the image points with the generators of the identifications. The point $\vec{x}'$ has first neighbor images at locations $\vec{y}_k=g_k\vec{x}'$ and second neighbor images at locations $\vec{y}_{k_2k_1}=g_{k_2}g_{k_1}\vec{x}'$, etc. More concisely, the images out to order m can be written as

$$\vec{y}_{k_m,\dots,k_1}=\prod_i^m g_{k_i}\vec{x}'(\hat{n}'). \tag{3}$$

The image point which lands closest to $\vec{x}(\hat{n})$ determines $d_{\min}$. Note that all of the effects of topology appear only in the minimization of the separation between the two points. Thus, the correlation function can be approximated using only a knowledge of the identifications that compactify the space: the very relations that are used to specify the topology.

Our approximation is closely related to the method of images employed in Refs. [9]. The correlation function computed by the method of images is a sum over *all* of the copies of the image points in the simply connected space with the same curvature,

$$C(\hat{n},\hat{n}') = \lim_{r_* \to \infty} \sum_{\gamma_i} C^U(d(\hat{n},\gamma_i\hat{n}'))$$
$$- \frac{4\pi}{V} \int_0^{r_*} dr \ \sinh^2 r C^U(r), \qquad (4)$$

where the second term is a regularizer introduced to control the exponential proliferation of images, particularly on $\mathbf{H}^3$, as the radius r_* increases relative to the volume of the fundamental domain, V [9]. The γ are composite elements of the group Γ. Our approximation amounts to keeping only the dominant term in the sum over images. Maintaining the first term is by far less cumbersome than summing an infinite number of terms and fares well in approximating the exact correlation function. The approximation is also quite valuable for our purposes since we are able to easily include the essential effects of the smoothing across the horizon at the time of last scattering and the relevant microphysics at work over small separations. The small-scale physics at the time of last scattering is important for distinguishing topologically lensed images from fictitious correlations as explained in Sec. II B. The physical processes operating at last scattering can in principle be folded into the method of images to refine our approximation and sharpen the focus on our pictures of geometry. The thickness and velocity of the surface of last scatter will also induce additional corrections. A test of our approximation when applied to the flat geometries is given in detail in Sec. II B.

Given an estimate of the full four-dimensional $C_{\mathcal{M}}(\hat{n},\hat{n}')$, we could build realizations of a map of $\delta T(\hat{n})/T$ for any topology, even without the eigenmodes. A given universe would be obtained by a random realization of a Gaussian-distributed variable with a mean $\langle \delta T(\hat{n})/T \rangle = 0$ and variance $C_{\mathcal{M}}(\hat{n},\hat{n}')$. However, we can do better. As $C_{\mathcal{M}}(\hat{n},\hat{n}')$ is a function on two copies of the sky, it necessarily must be calculated numerically for N_{pix}^2 values, where N_{pix} is the number of pixels into which the sky is divided. This is cumbersome, if not practically impossible, to carry out for many topologies on a reasonably finely grided sky map, particularly if we aim at the resolutions expected of future CMB satellite missions. Furthermore, many of the peaks of this function occur at values where $\hat{n}$ and $\hat{n}'$ are separated by a small angle on the sky. Since these points would be close together regardless of global topology, much of the base space of $C_{\mathcal{M}}(\hat{n},\hat{n}')$ is useless in discriminating between topological properties of cosmological models.

Instead of building full $\delta T(\hat{n})/T$ maps, we build selective correlation maps. An illustrative example is the antipodal map constructed by evaluating the correlation function at antipodal points along the sky,

$$A(\hat{n}) \equiv C_{\mathcal{M}}(\hat{n}, -\hat{n}). \qquad (5)$$

In a simply-connected universe $A(\hat{n})$ would produce on average nothing more than an overall monopole. Fortuitous correlations may appear at random in a given realization but there would be no defining structure. In a universe with compact topology a great deal of structure can be surveyed by means of this one simple correlation. While the best analysis for any particular topology will make use of the full correlation function, the antipodal map will prove to be a most useful survey tool. To get a feel for the way in which correlations reflect global topology, we make a gallery of correlated spheres first for all flat topologies and then for a few choice compact hyperbolic spaces. We also consider correlations under symmetries other than antipodal as the specific space demands. In order to represent the correlations as 2D maps we consider correlations of the form

$$C_g(\hat{n}) \equiv C_{\mathcal{M}}(\hat{n}, g\hat{n}/\|g\hat{n}\|), \qquad (6)$$

where again g is an element of the group Γ. For the compact hyperbolic spaces, we also correlate an arbitrary point with the rest of the surface of last scatter. In many ways these point-to-sphere correlations, are the most promising. They very dramatically reveal geometric patterns and they do not require any foreknowledge of the symmetries of the space.

II. THE COSMIC ZOO

A. Flat topologies

Compact flat spaces have already fallen out of favor as small universes. The first suspect for investigation was the simplest hypertorus [14]. The fundamental domain is a parallelepiped with opposite faces identified in pairs. As shown by Stevens, Scott and Silk [15], the square hypertorus suffers a sharp truncation of long wavelength power in temperature fluctuations, too sharp to be consistent with COBE observations unless the box is larger than about 40% of the observable universe. Later, anisotropic tori were studied in Refs. [16] using symmetry methods, and were similarly bound. The tightest limits on an equal-sided square hypertorus were obtained in Ref. [9] using the method of images, placing the topology scale just beyond the observable universe with $h \geqslant 2.19\Delta\eta$ where h is the length of the side of the square and $\Delta\eta$ is the conformal time since last scattering.

With the universal covering space of $\mathbf{E}^3$, there are only five more orientable, compact spaces that can be constructed [18]. Three are built by identifying the faces of a parallelepiped with relative twist (see Fig. 10), and two are constructed by identifying the faces of a hexagonal prism with the prism faces twisted by $2\pi/3$ or $\pi/3$ relative to each other before being identified. In Refs. [6,17], we derived the eigenmode spectrum explicitly for all twisted cases and showed that the angle-averaged power spectrum is incompatible with COBE for equilateral spaces unless the universe was very large, if
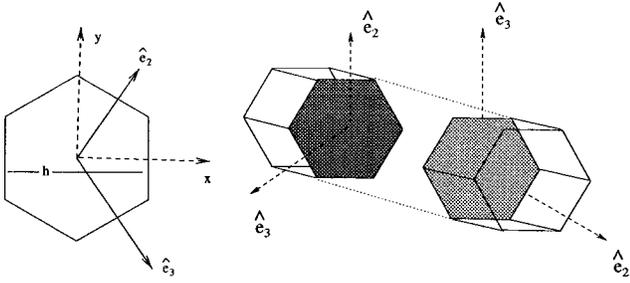
FIG. 2. The hexagonal geometry. The prism face is glued with a twist of $2\pi/3$ to create a topology distinct from the hypertorus.

not actually infinite (i.e. topological identification scale $\geqslant 80\% \Delta \eta$). The compact flat spaces are thus of limited interest, although polyhedra with sides of disparate lengths may still be viable.

However, since we do have eigenmodes for all flat topologies [6], these topologies are important testing grounds for any method which attempts to circumvent the eigenvalue problem. We therefore use $\mathbf{E}^3$ to test our real space approximation before moving on to compact topologies of $\mathbf{H}^3$.

For illustration, we spend time explaining the features in the markings for a $2\pi/3$-twisted hexagonal prism. The manifold is $\mathbf{E}^3/\Gamma$ with Γ the group of instructions for identifying the faces of the hexagon. Define a coordinate system for which $\hat{e}_1$ is orthogonal to the hexagonal face and the non-orthogonal vectors $\hat{e}_2, \hat{e}_3$ span the face as in Fig. 2. Γ is generated by $\{g_1, g_2, g_3\}$ where g_1 generates a rotation through $2\pi/3$ about the $\hat{e}_1$ axis combined with a translation orthogonal to the hexagonal face through a distance c, g_2 effects a translation along $\hat{e}_2$ through h, and g_3 effects a translation along $\hat{e}_3$ also through h. Another way to visualize $\mathbf{E}^3/\Gamma$ is to glue copies of the fundamental domain together according to the identification rules. In this way $\mathbf{E}^3$ can be completely tiled with layers of hexagons separated by the length of the prism direction.

We can use these symmetries to build the discrete spectrum of eigenmodes which describe fluctuations on this space as was done in Ref. [6]. Using these modes a typical map of $\delta T(\hat{n})/T$ for a simulated compact hexagonal universe can be created. We show this for comparison in Fig. 3. There is something at work in the map of $\delta T(\hat{n})/T$ but it is hard to define.

If, however, we inspect the idealized zero-variance antipodal map, the pattern jumps out at us. These antipodal
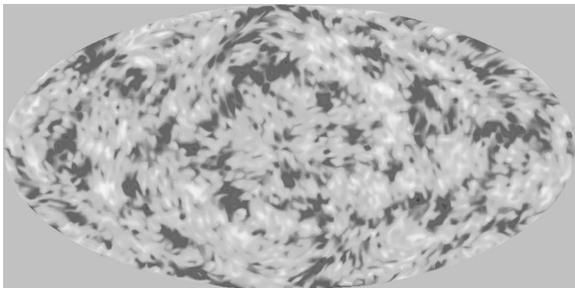
FIG. 3. A typical map of $\delta T/T(\hat{n})$ in a hexagonal prism with $h = 0.8 \Delta \eta$.
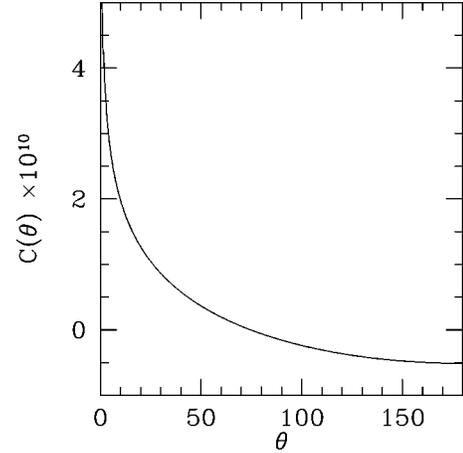
FIG. 4. $C^U(\theta)$ for a flat, COBE normalized CDM cosmology. Note that the correlation becomes negative due to the definition of $\delta T/T$.

maps were built with our approximation and *did not require the full mode solutions*. We locate a point on the sphere of last scattering (SLS) $\vec{x} = \Delta \eta \hat{n}$ and compare the correlation of that temperature with its antipodal point $\vec{x}' = -\Delta \eta \hat{n}'$. If the universe were simply $\mathbf{E}^3$, that is, flat and unconnected, then these points should be totally uncorrelated on average. Given that this space is multiconnected, the two opposed points may in fact be close together as demonstrated for the 2D surface of Fig. 1. We approximate the correlation between antipodal points as the correlation that the points would have in a simply connected space given their minimum separation as in Eq. (1). Antipody is then approximated as

$$\langle A(\hat{n}) \rangle \simeq C^U[d_{\min}(\vec{x}(\hat{n}), \vec{x}'(-\hat{n}))] \tag{7}$$

where $C^U(\theta)$ is obtained from CMBFAST [19] for a standard, flat CDM cosmology ($\Omega_b = .05, \Omega_c = .95, H_0 = 50$ km s^{-1} Mpc^{-1}) with the dipole component calculated as per a flat power spectrum. This is illustrated in Fig. 4. We minimize the distance by first taking the image of these points under the action of the generators of the group Γ until we relocate them within the fundamental domain. Leaving one of these relocated points fixed, we consider all images of the second point that lie within one of the nearest neighbors of the fundamental domain, and choose $d_{\min}$ as the shortest distance from the first point to one of these images. Note that only by considering all of these images, including those that are diagonally located relative to the fundamental domain, can we be sure that our definition of distance depends on the overall topology of the space rather than on the particular coordinates that we use to fix the fundamental domain. This method results in an overall monopole component of the antipodal map which we wish to discard. We simply remove the monopole as calculated from the antipodal map alone, with the understanding that this is to be compared with a measured map that is similarly normalized.

It is customary to use the Aitoff projection (as in Fig. 3) to view the map of $\delta T(\hat{n})/T$ so as to see the entire sky. For the antipodal map we prefer the orthographic projection which shows the genuine shape of the surface of last scatter-

FIG. 5. Orthographic projection of A(n̂) at a resolution of 20 arcminutes for a hexagonal prism with $h=b=c=0.8\Delta\eta$. The observer is at the origin.

ing. In this three-dimensional view, the sky pattern appears to lie on a sphere. No information is lost by limiting ourselves to a view of only half the sky at a time since A(n̂) is by definition symmetric under π.

There is clearly a hexagon in the antipodal map. The intersection of the hexagonal layers with the spherical surface of last scattering defines rings centered on the prism direction and are clearly picked out by A(n̂) (see Fig. 5). The rings of correlated spots occur since the correlation between points on the sphere of last scattering separated by π for this geometry is the same as the correlation between opposites sides on a circular slice through the sphere taken along the hexagonal plane, as demonstrated in Fig. 6. The bright primary spots are identical points at the core and are just correlated away from the center. In addition to these identical images, there are also secondary spots picked up due to the correlation of regions which just near each other.

These rings of structure are not the circles of the sky of Ref. [8]. As pointed out there, pairs of identical circles occur in the microwave sky due to the intersection of the surface of last scattering with copies of itself. None of the circles are located by A(n̂) for the $2\pi/3$ twist because none of the circles in this space are paired under a π-symmetry. For rings separated along the prism direction by multiples of $3c$, the hexagonal faces have completed a full rotation and antipody compares one point to its opposite face. We continue to call the concentric collections of spots in the correlated A(n̂) maps ''rings'' and we reserve ''circles'' for intersections of the copies of the surface of last scattering with itself. So, the primary spots on a given ring lie on different pairs of circles in the sky. The rings of secondary spots do not lie on circle pairs.

As the topology scale gets smaller, there are more rings of patterns and the first ring appears closer to the caps as shown in Fig. 7.

The size of a spot will be set by the Silk damping which smooths fluctuations on small scales. For separations which exceed this length, we expect correlations quickly to die off. Since the Silk damping scale is smaller than the horizon size at the time of decoupling we expect the angular size of these spots to be too small for COBE to have detected. The beam smearing in the COBE experiment would dilute a spot over such a large angle that these bright markings would be below
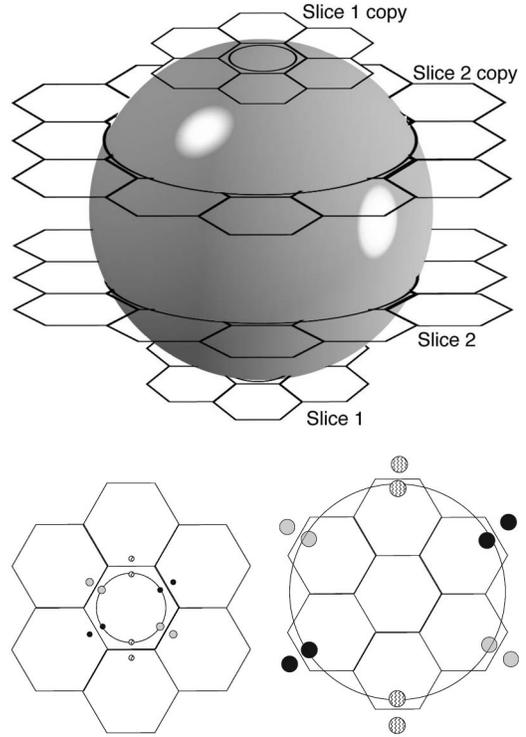
FIG. 6. The surface of last scatter intersects the layered tiling of flat space. Each full tile represents a copy of the fundamental domain. Slice 1 is represented on the lower left and slice 2 on the lower right. The dots show correlated points picked up in the antipodal map and explain the emergence of the hexagonal geometry in Fig. 5.

the signal to noise sensitivity of the detector. However, any experiment with high enough resolution and sensitivity to probe the Doppler peaks will be able to resolve these patterns on the sky. The planned missions MAP and *Planck Surveyor* would thus be able to detect the universe's spots.

The other topology built from the hexagonal plane tiling involves a relative twist of the prism face through $\pi/3$. As seen in the left-most panel of Fig. 8, there are again correlated spots on rings. When we make the space sufficiently small so that at least three copies of the fundamental domain fit within the SLS the first pair of circles appears in $A(\hat{n})$, as shown in the right-most panel of Fig. 8.
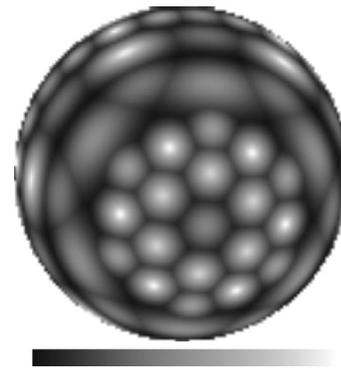
FIG. 7. Orthographic projection of A(n̂) for a hexagonal prism with $h=b=c=0.6\Delta\eta$.
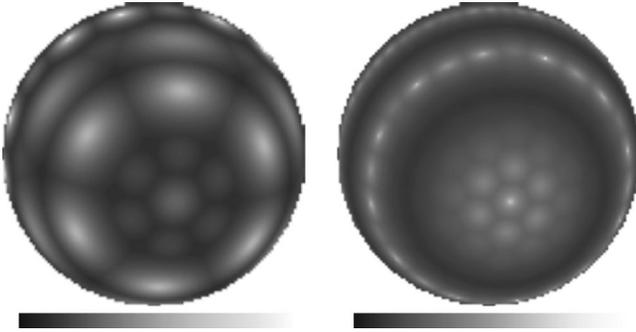
FIG. 8. A(n̂) for a hexagonal prism with a $\pi/3$ twist $h=c$ $=0.75\Delta\eta$; there are no circles. To the right the z direction is .24 while $h=1$; there are circles.

The other four topologies are built from a parallelepiped as the fundamental domain, as for the simplest hypertorus. No circles will be located by A(n̂) for the hypertorus, which is not to say that the hypertorus has no circles, just that none of the pairs of circles are rotated by π relative to each other. Since the hypertorus does not involve any rotations of the faces, all three directions are picked out equally by antipodal pairings, as seen in the small torus of Fig. 9. The square geometry of the fundamental domain is blatantly traced out by the correlated spots leading to the disco ball effect.

For the twisted parallelepipeds, A(n̂) will locate the axis of symmetry along which the faces are twisted. The correlated spots still trace out the symmetric square of the equilateral untwisted directions, as shown in Fig. 10. For the $\pi/2$ twisted space, the circles appear in A(n̂) if more than two copies of the fundamental domain fit inside the observable universe. At least one pair of circles will appear always for the π-twisted space as well as for the last compact topology built by gluing a parallelepiped by a series of diagonal translations and π twists.

The menagerie in this flat zoo is a testament to the influence of geometric patterns on the universe's markings. An antipodal correlation is just one statistic but note how clearly antipodal correlations reveal the other symmetries of the space. For instance, the prism direction perpendicular to the hexagonal face is clearly identified. Once the symmetries of the space do begin to become apparent, the future data on the CMB can be systematically scanned for correlations under other symmetries of a given topological space:

FIG. 10. A(n̂) for a $\pi/2$-twisted space.

$C_{\mathcal{M}}(\hat{n}, g\hat{n}/\|g\hat{n}\|)$. In this way the entire fundamental group Γ can be isolated, thereby determining the full geometry of the space, as was also suggested in Ref. [20].

The indicator A(n̂) is particularly convenient because it can be visualized on an half-sphere without the specification of a particular axis, but once an axis of symmetry is chosen, correlations at other angular separations can similarly be examined. As an example of such a correlation, we consider $C_{\mathcal{M}}(\hat{n}, \hat{n}')$ where we merely compare the point (x,y,z) to the point $(x,y,-z)$ for the hypertorus of size 0.4 of the SLS. We assume that this axis has been identified by examining the overall antipodal properties of the sky. We expect this correlation to pick up circles and it does, as demonstrated in the Fig. 11.

As another example we compare, for the $\pi/2$-twisted space of size 0.4 the radius of the SLS, the correlation between two points separated by a rotation of $\pi/2$ around the x axis. In Fig. 12 we display the result of applying the correlation function

$$C_{\mathcal{M}}[d_{\min}(\vec{x}(\theta,\phi), \vec{x}'(\theta,\phi+\pi/2))]. \tag{8}$$

B. Observing the universe's spots

Our topological zoo of maps makes a compelling visual argument for a pattern-driven approach to the search for cosmic topology. Nevertheless, they are still only ensemble-averaged images calculated using an approximation method. As the real microwave sky contains no such averages or approximations, we are left wondering if we should believe our eyes.

FIG. 9. A(n̂) for the torus with $h=b=c=0.31\Delta\eta$.
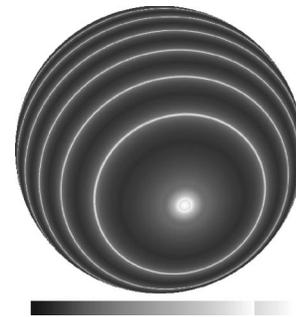
FIG. 11. The sphere of correlations $C(\hat{n}(x,y,z), \hat{n}(x,y,-z))$ for the hypertorus. The topology scale is $0.4\Delta\eta$.
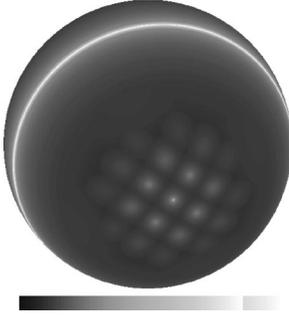
FIG. 12. The correlated sphere comparing points on the surface of last scatter with points related by a $\pi/2$-twist around the z-axis. The space is a $\pi/2$-twisted square with sides of length $0.4\Delta\eta$.

In this section, we address the accuracy of our method by comparing our approximate maps with exactly calculated ensemble-averaged maps as well as with simulated realizations of the microwave sky. We consider the flat hypertorus which has a simple eigenmode decomposition of the temperature fluctuations,

$$\frac{\delta T}{T}(\hat{n}) \propto \sum_{\vec{k}} \hat{\phi}_{\vec{k}} \exp(i\Delta\eta\vec{k}\cdot\hat{n}), \qquad (9)$$

with $\vec{k} = 2\pi(n_x/h, n_y/b, n_z/c)$. The $\hat{\phi}_{\vec{k}}$ are primordially seeded Gaussian amplitudes that obey the reality condition $\hat{\phi}_{\vec{k}} = \hat{\phi}^*_{-\vec{k}}$ and as an ensemble define the spectrum

$$\langle \hat{\phi}_{\vec{k}} \hat{\phi}^*_{\vec{k}'} \rangle = \frac{2\pi^2}{k^3} \mathcal{P}(k) \delta_{\vec{k},\vec{k}'}. \qquad (10)$$

With this decomposition we can construct the correlation function between any two points on the sky as

$$C(\hat{n},\hat{n}') = \left\langle \frac{\delta T}{T}(\hat{n}) \frac{\delta T}{T}(\hat{n}') \right\rangle$$

$$\propto \sum_{\vec{k}} \frac{\mathcal{P}(k)}{k^3} \exp(i\Delta\eta\vec{k}\cdot(\hat{n}-\hat{n}')). \qquad (11)$$

The antipodal correlation on the hypertorus is the simple case, $C(\hat{n}, -\hat{n})$, and

$$\langle A(\hat{n}) \rangle \propto \sum_{\vec{k}} \frac{\mathcal{P}(k)}{k^3} \exp(i2\Delta\eta\vec{k}\cdot\hat{n}) \qquad (12)$$

up to an overall normalization. This is nothing more than a Fourier transform of the power spectrum, and can be computed exactly.

In Fig. 13 we compare the results of our approximation with the exact eigenmode decomposition of Eq. (12) for the case of the hypertorus with $h = b = c = 0.8$. In both calculations, we take a simple flat $[\mathcal{P}(k) = 1]$ power spectrum with no additional physics added.

In both maps the small-scale structure and location of the spots are identical, but in the approximate map the large-scale features of the spots are smeared out. This smearing
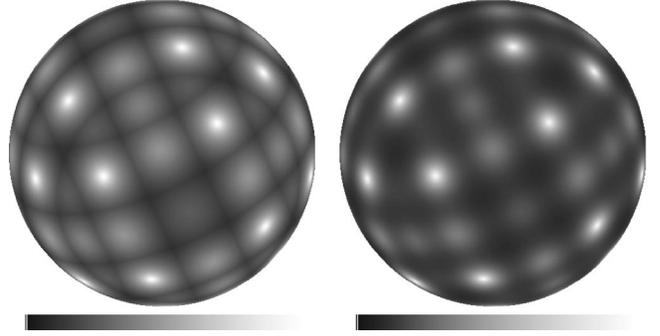
FIG. 13. A comparison of the real-space approximated antipodal map (left) with the exact ensembled-averaged map (right) for a torus space with $h = b = c = .8\Delta\eta$.

stems from the fact that our approximation does not incorporate the damping of power at low wavenumbers due to the discretization of eigenmodes on the compact space. Thus $C^U[d_{\min}(\vec{x}(\hat{n}), \vec{x}'(\hat{n}'))]$ falls off more slowly than the corresponding correlation function on the compact space.

This discrepancy can be remedied by replacing the C^U with an angular correlation function from which the lowest multipoles have been removed. In the case of a $h = b = c = 0.8$ space, the damping is well approximated by removing the dipole, quadrupole, and octopole terms [17]. This results in the approximate map shown in Fig. 14, which is quite close to the exact result. In principle, the broadening of the spots can also be removed by including more terms in the method of images expansion, Eq. (2). In practice, however, a cumbersome number of terms have to be included in order to begin to approach the exact result, with the maps actually getting worse before they get better.

The question remains how to analyze real data so as to extract patterns with confidence. It is customary in an analysis of CMB observations to take angular averages in Fourier space. All standard methods thus smear out the very patterns we seek. Instead we advocate that the correlation maps be treated as real space pictures of geometry. As such, they are akin to pictures of a galaxy or to observations of gravitationally lensed images.

All of the previous correlation maps are ensemble averages. Since we have only one universe to observe and only
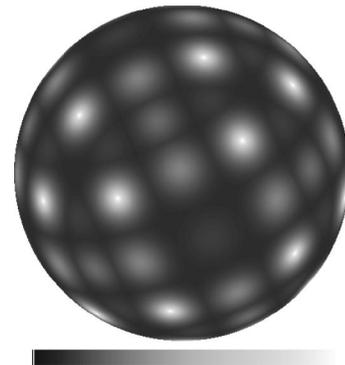
FIG. 14. Real-space approximated antipodal map, calculated from a flat power-spectrum in which the dipole, quadrupole, and octopole have been removed.
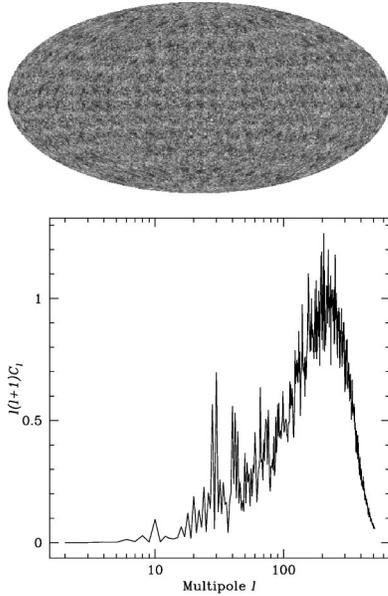
FIG. 15. Upper panel: the unsmoothed numerical CMB data with 1024×513 pixels for a small square hypertorus with side of length $0.2\Delta\eta$. Lower panel: the power spectrum for this simulation.

one realization of the data we might worry that cosmic variance would drown out any of the features of topology in a given realization. We are unable to combat cosmic variance by averaging over the sky since it is precisely such averaging which we are trying to avoid. We have numerically simulated high-resolution observations of a toroidal universe to demonstrate what future satellite observations will offer. Cosmic variance is not a terrible hindrance and we are able to extract the correlated information from the high-resolution simulations.

The map of $\delta T(\hat{n})/T$ at the top of Fig. 15 is a simulation of an all-sky map generated using the explicit eigenmodes of (9). The physical processes at work on very small scales were modeled so as to emulate the Doppler peaks of a flat CDM universe. To obtain fairly accurate maps we have to keep account of the physical processes at the epoch of decoupling which determine the shape of the spectrum. At decoupling, the comoving length of the horizon is $\eta_{dec} \simeq 10^{-2}\Delta\eta$, which is presumably far smaller than the dimension of our fundamental domain. The causal processes that modulate the spectrum are therefore not modified by the compact nature of the space. In this case we can use a suitable function for $\mathcal{P}(k)$ which is able to reproduce the height and position of the first Doppler peak in a flat CDM universe. The function we choose is the following:

$$\frac{\mathcal{P}(\kappa)}{\kappa^3} = (\kappa^{n-1} + \kappa^{n+1} + \kappa^{n+3})\exp(-\kappa^2/4) \qquad (13)$$

where $\kappa = 10^{-2}k\Delta\eta$ and n is the primordial fluctuation spectral index. We show this function in Fig. 16. In the same figure we also show the k-range covered by the model we examined. With the power spectrum of Eq. (13), the relative height of the first Doppler peak and the Sachs-Wolfe plateau are in good agreement with a flat CDM model for $0.8 \leqslant n$
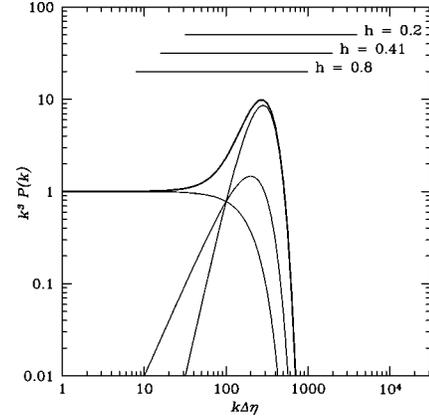
FIG. 16. The power spectrum as a function of $k\Delta\eta$.

$\leqslant 1.2$. As reported in [6], the lower limit on k is fixed by the dimensions of the fundamental domain, while the upper limit is constrained by the resolution grid in **k**-space used to generate a given realization. We used a grid of $n_x n_y n_z = 256^3$ elements in **k**-space which we fast-Fourier transformed back into real space to calculate our $\delta T(\hat{n})/T$ spectra. The maximum wavenumber for a given realization is $k_{max} = n_x \pi/h$. It is apparent from Fig. 16 that it is unnecessary to go beyond this resolution limit to probe down to the accuracy of our approximate power spectrum.

To obtain the angular power spectrum, $C_l = \Sigma_m |a_{lm}|^2/(2l+1)$, we decompose the temperature fluctuations into spherical harmonics, $\delta T(\hat{n})/T = \Sigma_{lm} a_{lm} Y_{lm}(\hat{n})$, using a modified version of the fast code developed by Muciaccia *et al.* [21]. The power spectrum of the simulation can be seen at the bottom of Fig. 15. Notice the enhancement of power due to the multiple copies of the fundamental domain, a feature already noted in Ref. [17]. While the C_l's certainly do not contain all of the information in a map of $\delta T/T$ in a universe with multiconnected topology, the spectrum does reveal the essential behavior of $\delta T/T$ at very high l's where topology is less influential.

The leftmost panel in Fig. 17 is the antipodal map from the data smoothed on scales of $1.5°$. We smooth the map of Fig. 15, as though the data were convolved with an experimental beam, before taking the product map. The ensemble average computed from Eq. (12) is shown in the rightmost
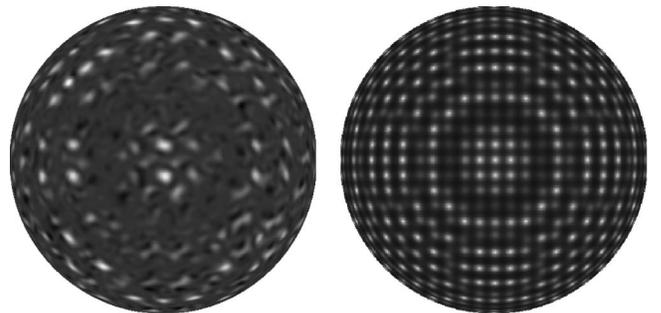
FIG. 17. The simulated data shown in Fig. 15 is smoothed on scales of $1.5°$. The antipodal map (left) is then read off the smoothed data and compared with an ensemble average (right).
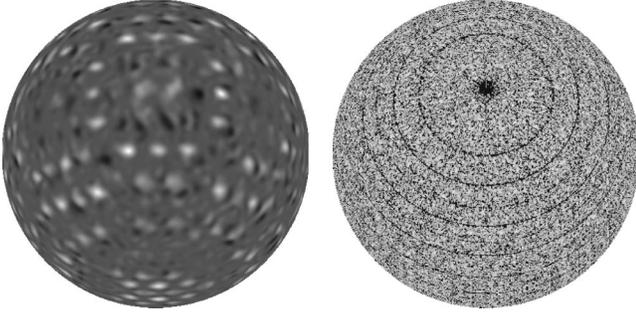
FIG. 18. On the left is the correlated sphere $C_z(\hat{n})$ defined in Eq. (14) read directly off the numerical data. On the right the quantity $\xi_z(\hat{n})$ of Eq. (15) is plotted to draw out the circles.

panel of Fig. 17. Clearly, the realization shows the structure of the ensemble average. While this small universe can be ruled out with the COBE data due to the conspicuous lack of power on small scales [15,6], the pattern would go undetected in the existing satellite data. If we had smoothed on scales of 7° to emulate the COBE experiment, any definitive pattern would have been washed away. The much higher resolution of MAP and *Planck Surveyor* is required to measure the universe's spots.

The very small space was chosen for dramatic effect. Since these spaces sample low l modes more sparsely, there is less cosmic variance in some sense and the patterns are easier to detect. The large spaces can suffer more contamination from low l modes. To recover the bare information in the ensemble averages, the low l modes may need to be cleaned from the larger spaces.

We also consider the correlation which compares $\hat{z} \rightarrow -\hat{z}$, as this is a true symmetry of the space. If we align the fundamental domain with the $\hat{z}$ axis of the SLS, then the correlation compares points in the direction $\hat{n}(\theta, \phi)$ with points in the direction $\hat{n}'(\pi - \theta, \phi)$:

$$C_z(\hat{n}) = C((\theta, \phi), (\pi - \theta, \phi)). \quad (14)$$

Notice that even in a universe with no topology there will be some structure in such a correlation function. The equator so defined is always compared with itself and so shows more correlations than the poles even without multiconnected identifications. Since this is an actual symmetry of the hypertorus we should find 10 circles in one hemisphere for the small space of size $h = 0.21\Delta\eta$. We pick up nine circles at latitudes 64°, 53°, 44°, 37°, 30°, 24°, 17°, 11° and 6°, and ten if we include the one identified point at the poles, as shown in Fig. 18 (compare with Fig. 11). It is difficult to see that these spots do in fact lie on fully correlated circles. After all, the maps only represent the simple product $\delta T(\hat{n})\delta T(\hat{n}')/T^2$. A measure of the correlations across the pairs of circles would draw out the feature more crisply (see also, in this connection, the statistic suggested in Ref. [8]). To illustrate, we plot the quantity

$$\xi_z(\hat{n}) = \left(\frac{\delta T(\theta, \phi)}{T} - \frac{\delta T(\pi - \theta, \phi)}{T} \right)^2 \quad (15)$$
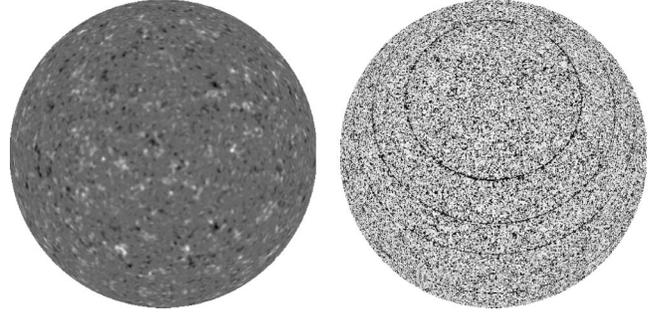
FIG. 19. On the left is $C_z(\hat{n})$ read directly off the numerical data for the larger torus of size $0.41\Delta\eta$ smoothed on scales of 0.5°. On the right $\xi_z(\hat{n})$ of Eq. (15) is plotted.

for the unsmoothed data, in the rightmost panel of Fig. 18. This measure of the temperature difference singles out the circles.

For a larger square torus of size $h = 0.41\Delta\eta$, the correlation $C_z(\hat{n})$ of Eq. (14) also finds faint circles. Figure 19 shows the occurrence of circles in the sky at latitudes of around 55°, 38°, 24° and 12°. The left figure is a map of the simple correlation function $C_z(\hat{n})$ of Eq. (14) smoothed at 0.5° while the right figure locates the circles more distinctly, without smoothing, by plotting the $\xi_z(\hat{n})$ of Eq. (15). The thin dark circles are the collection of identical points for which $\xi_z = 0$.

For contrast, we compare the predictions for a hypertorus with those for a simply-connected flat cosmos. Figure 20 shows a realization of the SLS for a flat CDM universe. The data is again smoothed on scales of 1.5°. The low l modes missing from the map in Fig. 15 are clearly present in an infinite universe. There is no evidence of a pattern in antipodal correlations, nor in the $C_z(\hat{n}, \hat{n}'(\vec{z} \rightarrow -\vec{z}))$, as demonstrated in the bland pictures of Fig. 20.
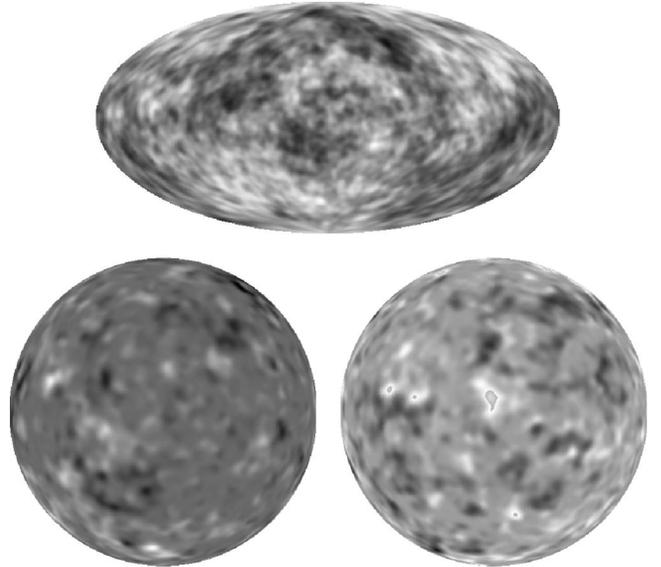
FIG. 20. Simulated CDM data for a universe with no topology. The standard map of the surface of last scatter is shown on the top. On the bottom left is the map $A(\hat{n})$ and on the bottom right is the map $C_z(\hat{n})$.

In general we suggest a two-step investigation to observe topological lensing as the data becomes available. Firstly, it is advantageous to smooth the data on some small scale. Correlations can then be read off more easily from the smoothed map. Secondly, the unsmoothed data can then be exploited to measure the temperature variation across the spot at the location indicated by the correlated signal. The measured spectra of the related spots can then be compared. If the spectra match, topologically lensed images have been measured: a correlation measure across two spots can be used to confirm lensed copies of a fluctuation. The small-scale structure of the two regions should be almost identical,[2] although large-scale effects such as the subtraction of the CMB dipole, or the integrated Sachs-Wolfe effect in open spaces may cause a difference in the mean temperature of the two patches. In practice, a generalization of Eq. (15) such as

$$\xi(\vec{x}) = \left(\frac{\delta T(\vec{x} - \vec{x}_{\text{spot}})}{T} - \frac{\delta T(\vec{y} - \vec{y}_{\text{spot}})}{T} \right)^2 \qquad (16)$$

where the temperature fluctuations are defined with respect to the local mean temperatures of the spots, should do well in confirming lensed copies of fluctuations.

As we improve our understanding of the correlation function on short scales we might determine the spectrum of each of these spots and use this information to distinguish fictitious correlations from the real thing. In an actual realization, all of these correlated spots will be there under a web of spurious correlations due to cosmic variance. These random correlations can be distinguished much as foreground sources are distinguished from the galaxies they occult. Spurious correlations will not be distributed on rings, nor will they have the characteristic size and spectrum of the topological correlations. Cosmic variance as a form of cosmic noise could thus in principle be subtracted off the maps. Again, the task is similar in spirit to distinguishing the gravitationally lensed images of a quasar from other unrelated or foreground sources.

III. THE HYPERBOLIC ZOO

We turn now to the application of our correlated spheres to compact hyperbolic universes. Compact hyperbolic spaces are inherently chaotic. The exponentially deviating trajectories of geodesic motions on a space of negative curvature mix and fold chaotically through the space as they exit and enter the multi-faceted fundamental domain. Chaos endows these spaces with many intriguing properties, including fractal structures within the pattern of entangled geodesics. The patterns inscribed in these skies thus promise to be intricate. Primordial quantum fluctuations which ultimately seed the hot and cold spots are described by quantum chaos for which there are very different predictions than for nonchaotic quan-

tum systems [22]. The assumption of a flat, Gaussian seeded spectrum of perturbations may be a poor one.

While complicated, these spaces are not obscure. There is a countable infinity of topologically distinct compact **H**^{3} spaces, although they have yet to be completely classified [23]. Furthermore, observations favor a universe with subcritical density. There is therefore considerable interest in understanding the predictions for these spaces. Regardless of how predictive maps are produced, the ultimate question is, how do we analyze the CMB data to search for topology. Canonical treatments rely on angular averages which smear out patterns and a likelihood analysis based on Gaussian statistics. While this may have some restricted meaning, it is dangerous to draw precise conclusions from a Gaussian isotropic probability distribution when the space itself destroys isotropy and the primordial spectrum is unknown. Furthermore, it requires a case by case analysis and may even depend on the location of the observer.

This implies that a statistical analysis of the data requires a model template. If the universe is not a perfect manifold of constant curvature the template match is lost. Instead of asking the statistical fit of the data to an infinite number of models we can just take a picture of the sky and from this obtain a picture of correlated maps. As already argued, the spectrum of the spots can be measured to judge if we are really looking at the topological lensing of the horizon at the time of decoupling. The idea of combing the data for circles in the sky also shares the model independence feature and motivation.

We apply our method to two small hyperbolic topologies, the Weeks space and the Best space, named after their discoverers. The Best space is a compact hyperbolic manifold obtained by identifying the twenty faces of a regular icosahedron [24]. The Weeks space [25] has a more complicated fundamental domain with 18 faces and is of particular interest since it is currently the smallest compact hyperbolic space known.

A. Strong patterns in a Weeks space

It is advantageous to consider **H**^{3} embedded as a 3D surface in a 4D Minkowski spacetime. The universal cover **H**^{3} is then a pseudosphere and the 4D coordinates are restricted to the 3D surface with pseudoradius -1,

$$-u_0^2 + u_1^2 + u_2^2 + u_3^2 = -1. \qquad (17)$$

The isometries of **H**^{3} can then be written as 4×4 matrices of the special Lorentz transformations. The coordinate transformation

$$u_0 = \cosh r$$

$$u_1 = \sinh r \sin \theta \cos \phi$$

$$u_2 = \sinh r \sin \theta \sin \phi$$

$$u_3 = \sinh r \cos \theta \qquad (18)$$

---

[2]The sphere of last scatter cuts through the same 3D volume differently, so even if a point is identical to another on the SLS, the surrounding small region can be a slightly different sample of the 3D patch.

recovers the cosmologically familiar form of the 3D metric distance in comoving coordinates,

$$ds^2 = dr^2 + \sinh^2 r(d\theta^2 + \sin^2\theta d\phi^2). \quad (19)$$

The geodesics take on a particularly simple form [26] in the Minkowskian space. For simplicity, we tended to leave the Earth at the origin. For completeness, we mention how to move the Earth away from the center of the universe. If we align the Earth with the z-axis at position $u_e^\mu = (u_e^0, 0, 0, u_e^3)$ we can Lorentz boost the Earth to the origin with the transformation

$$\Lambda = \begin{pmatrix} \gamma & 0 & 0 & -\gamma\beta \\ 0 & 1 & 0 & 0 \\ 0 & 0 & 1 & 0 \\ -\gamma\beta & 0 & 0 & \gamma \end{pmatrix} \quad (20)$$

and $\gamma \equiv u_e^0$ and $\gamma\beta \equiv u_e^3$. A photon observed in the direction $\hat{n}$ has $\hat{v} = -\hat{n}$ and thus originated on the SLS at coordinates

$$u = \Lambda^{-1} \begin{pmatrix} \cosh \Delta\eta \\ \hat{n} \sinh \Delta\eta \end{pmatrix}. \quad (21)$$

This can easily be generalized to an arbitrary location with an arbitrary Lorentz boost.

The radius of the SLS, $\Delta\eta$, depends on the value of Ω_0 and the redshift of last scattering. In general,

$$\eta = \text{arccosh}\left(1 + \frac{2 - 2\Omega_0}{\Omega_0(1+z)}\right) \quad (22)$$

in units of the curvature radius. The volume of the SLS is

$$V_{SLS} = \int \sinh^2 r \, dr \, d\Omega$$
$$= \pi(\sinh(2\Delta\eta) - 2\Delta\eta). \quad (23)$$

The volume of the SLS grows exponentially with time. Therefore, many more copies of the fundamental domain can be contained within a surface of last scatter. The number of copies is a topological invariant, quite unlike in flat space. In flat space, one is free to set the volume of the manifold relative to the volume of the SLS arbitrarily. This is not possible for $\mathbf{H}^3$, as is ensured by the rigidity theorem [27], which states that the volume in units of the curvature is fixed. A peculiar consequence is that the volume of a manifold is a topological invariant. In effect, if we measure topology we can refine our measure of the radius of the last scattering surface and thereby Ω_0. In other words, we can use topology to measure curvature.

In order to compactify the space, we consider the specific example provided by the Weeks space. The fundamental domain is a polyhedron with 18 faces and 26 vertices shown in Fig. 21 which was taken from *SnapPea*, a census of compact hyperbolic manifolds [28]. The Weeks space is the smallest
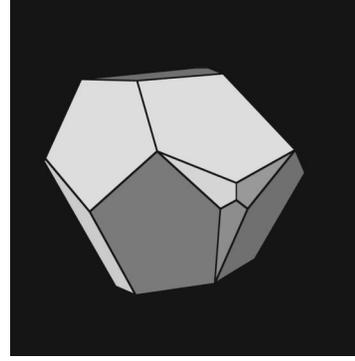
FIG. 21. The Dirichlet domain for the Weeks space.

3-manifold known with a volume of $\simeq 0.94$. With $\Omega_0 = 0.3$, and the redshift of last scattering taken to be $z = 1100$, so $\Delta\eta = 2.328$, we get $V_{SLS} = 150.64$, and so there are roughly 150 copies of this universe within the SLS. With $\Omega_0 \simeq 0.6$, $\Delta\eta \sim 1.5$ and there are only about 5–6 copies.

There are 9 identification rules to glue these 18 faces in pairs. The 9 g_i can be used to define a set of generators with many relations among them (such a set of generators was also used by Fagundes [29]). They are related to the words a, b of a much simpler presentation of the fundamental group $\{a, b : ababa^{-1}bba^{-1}b, abab^{-1}aab^{-1}ab\}$. We extract from *SnapPea* these nine face-pairing $O(3,1)$ matrices and their inverses out to 12 significant digits. It is necessary to use extremely precise matrices due to the chaotic flows. The sensitivity to initial conditions causes the image points to quickly be lifted off the pseudosphere if insufficient precision is used.

The image points are denoted by y^μ in Minkowski coordinates:

$$y^\mu_{k_n, \ldots, k_1} = \prod_i^n g_{k_i} u'^\mu$$

and $k_i = \pm 1, \ldots, \pm 9$. Since we number the g_k from 1–9, let g_0 be the identity so that $y_0^\mu \equiv u'^\mu$. We want to find the closest separation between u^μ and any of the image points y^μ. The $g_{k_i} \cdots g_{k_n}$ form words of length n where n is the highest order of the farthest neighbor.

Another way to count copies is to count periodic geodesics. The identification rules correspond to the minimal closed loop geodesics. The number of geodesics of length L goes as

$$N(L) \sim \frac{e^{hL}}{hL}$$

which is a result from chaos theory, with the Kolmogorov-Sinai entropy determined by the volume scale, $h \sim V^{-1/3}$. If we assume crudely that $L = nV^{1/3}$ so that n is the order of the neighbor, that is, the length of the word y^μ, then

$$N(n) \sim e^n / n.$$

So, for $\Omega_0 = 0.3$, the SLS encompasses roughly 150 copies of the fundamental domain and includes copies which are between 6 and 7 words away. For $\Omega_0 = 0.6$, the farthest neighbors are about 3 words from the origin. The 9 generators and their inverses combine to form 18^n words of length n but as a result of the many relations among the g_k, all but $N(n) \sim e^n/n$ of these are repeats. Scanning the 18^n possible images $N_{pix} \times N_{pix}$ times is a huge numerical demand. To manage the task we use the following numerical algorithm, which is analogous the scheme used in the flat cases:

(1) Move the point u on the SLS in towards the origin two steps to the image points $y^\mu_{k_2 k_1} = g_{k_2} g_{k_1} u^\mu$. Out of these 18^2 points, select the three nearest the origin.

(2) Move these 3 images two more steps and keep the one image nearest the origin so that it is essentially within the fundamental domain. Depending on how many neighbors fit within the SLS, step (2) can be repeated.

(3) Repeat the same steps to the point u' being compared. Both points should now be located within the fundamental domain.

(4) Keeping one image fixed within the fundamental domain, move the other within two neighbors until the distance between the two images is minimized.

(5) The geodesic distance on the pseudosphere is

$$d(y^\mu, y'^\mu) = \mathrm{arccosh}(y^0 y'^0 - \vec{y} \cdot \vec{y}'). \qquad (24)$$

We use this in our approximation

$$C_\mathcal{M}(\hat{n}, \hat{n}') \approx C^U[d_{\min}(\vec{x}(\hat{n}), \vec{x}'(\hat{n}'))], \qquad (25)$$

where we use the angular correlations obtained from the CMBFAST code, with $\Omega_b = 0.05$ and the remainder of the subcritical density is assumed to be made up of nonbaryonic dark matter.

It is important to note that in a negatively-curved cosmos there is, in addition to the Sachs-Wolfe effect on the surface of last scattering, an integrated Sachs-Wolfe (ISW) contribution to the perturbations. The ISW effect is due to the decay of the gravitational potential as the photons transit the space. Although we have not yet fully included the ISW effect, only the fluctuations on the largest scales should be affected whereas spots probe small-scale physics. On those scales where the ISW effect contributes the geodesics are deviating sufficiently so that photons that originated in the same vicinity quickly take different paths with different decaying gravitational potentials. Correlations will not therefore be enhanced. One might fear that topological correlations could be erased by the different histories of the two initially adjacent photon trajectories. Since the ISW effect does not effect the Doppler peaks in an infinite cosmos, it should leave the universe's spots unmarred. The next phase of investigation should include the ISW effect. Our maps correspond to data for which the lowest multipoles have been cleaned off.
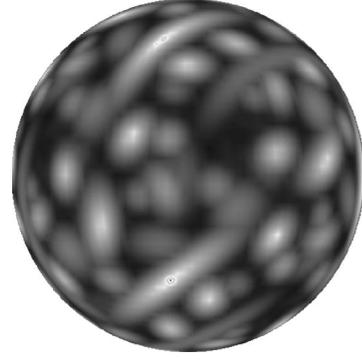
FIG. 22. An antipodal map for the Weeks space with $\Delta \eta = 1.5$.

An antipodal map for the Weeks space is shown in Fig. 22. There is clearly topological lensing evident in this map. The stripey features are significantly different from the geometric spots seen in the $A(\hat{n})$ maps of the flat spaces. Unlike all of the flat spaces, no obvious axis of symmetry is selected, which is to be expected given the geometry of the fundamental domain. The appearance of strong topological correlations in the future data and the absence of a clear axis of symmetry under antipody would implicate a compact and curved universe.

Another revealing correlation function for the hyperbolic spaces compares a random point with the rest of the surface of last scattering, $C(u^\mu, \hat{n})$, as shown in Fig. 23. This is unlike any correlation we have considered so far, but it can clearly be quite successful at uncovering geometric properties. As in the flat universes, the spots are likely spread out since we have not accounted for the discretization of the harmonics of the finite box which causes big dips in power at large modes, especially for such a small space. Again, the inclusion of a huge number of terms would be needed to incorporate this effect. We also compute $C(\hat{n}, g_8 \hat{n}/\|g_8 \hat{n}\|)$ in Fig. 24. This transformation combines a boost along the hyperbolic surface with a rotation.

B. The Best patterns

Best built three compact hyperbolic spaces by identifying the faces of an icosahedron possessing twenty triangular
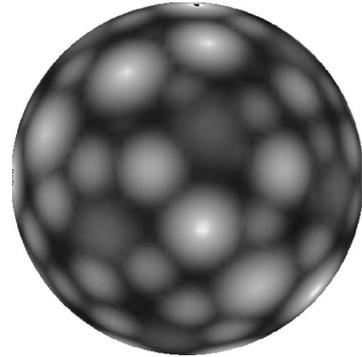
FIG. 23. Correlation with a random point and the rest of the sphere for the Weeks space with $\Delta \eta = 1.5$.
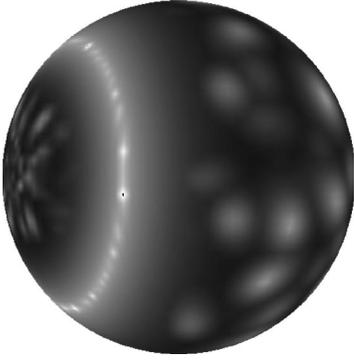
FIG. 24. The sphere correlated under the transformation g_8.

FIG. 26. The map of $A(\hat{n})$ for the Best space with $\Omega = 0.3$.

faces, as shown in Fig. 25. All of these spaces have volume $V = 4.6860342738$. The smallest geodesic ball which can encompass this space has a radius of radius $r \simeq 1.38$ while the largest sphere which can be inscribed within the icosahedron has radius $r \simeq 0.87$. For a rough estimate of the number of copies we count $N = V_{SLS}/V$. With $\Omega_0 = 0.3$, there are on the order of 32 copies of this Best space within the SLS.

The faces are identified with 10 generators, the matrix representations for which can again be found in *SnapPea*. The abelianized homology group is **Z/35**. Fagundes also studied this space and, in particular, the occurrence of periodic quasar images [30]. The other three non-isomorphic Best spaces with icosahedra as fundamental domains have different fundamental groups and homology groups of **Z/29** and **Z/2×Z/2**. To construct our maps, we follow the same procedure as detailed for the Weeks space.

The map of $A(\hat{n})$ is shown in Fig. 26. Antipody outlines pairs of identified triangular faces and also locates circles. Clearly a symmetry group for the Best space is located in this map. The cosmic soccer ball in Fig. 27 is the correlation of one point on the SLS with the rest of the sphere. The point happens to be very near the origin of one of the copies of the icosahedron. The patterns in the plot reflect the extreme symmetry of the fundamental domain and also hint at the fractal nature of the geodesics. Notice the five-pointed star surrounding the tetrahedron. In the triangular corners of the five-pointed star there appear to be six-pointed stars surrounding hexagons.

Both Figs. 23 and 27 are ensemble averages. To draw out the topologically lensed images in an actual observation, we need to define a quantity such as

$$\xi(\hat{n}) = \left(\frac{\delta T(\hat{n}_0)}{T} - \frac{\delta T(\hat{n})}{T} \right)^2 \tag{26}$$

where $\hat{n}_0$ is the point to be compared with the rest of the sphere. As detailed in Sec. II B, such a procedure locates candidate topologically lensed images. The spectrum across the candidate clone can then be measured and compared with that of the original point to ascertain if it is a good fit to a clone or nothing more than a random correlation.

As data from the planned satellite missions becomes available, the CMB can be scanned for any hidden geometric features. In the meantime, these correlated spheres show the huge potential for a pattern-oriented search of topological lensing.

Our real-space approximation allows one to calculate temperature correlations while avoiding the analytically intractable eigenvalue problem on compact hyperbolic 3-spaces. Once a candidate compact universe has been established, such templates are useful for deeper statistical studies [9]. However, an observational search for topology through large-angle temperature correlations can be made without a particular template being presupposed. This model indepen-

FIG. 25. The Dirichlet domain for the Best space.
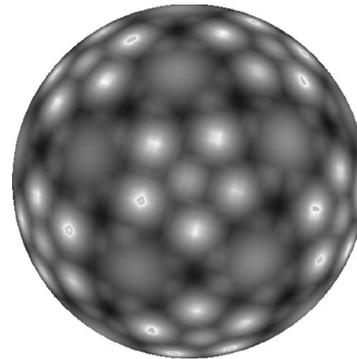
FIG. 27. The correlation of one point on the surface of last scatter with the rest of the sphere. The point is near the origin of one of the clones of the fundamental domain.

dence of a pattern-driven approach is particularly important because it allows us to take pictures even if the space does not have constant curvature, if observations depend strongly on the location of the observer, or if chaotic mixing leads to unusual primordial spectra. Since we cannot predict topology within existing theories, we need this flexibility.

While general relativity predicts the evolution of curvature, it does not specify the topology of space or of spacetime. Only a theory beyond Einstein's will be able to fully specify the geometry of the universe. Supergravity theories necessarily acknowledge the importance of topology and compact hyperbolic cosmologies have even recently been studied as a consequence of string theories [31]. However the universe was born, it was endowed with some topology and will have a place in our cosmic zoo. Astronomical studies of the topology of the universe may provide the most important insights into those aspects of the fundamental laws of Nature that dictated the global character of the space in which we live.

Geometry effects not just the large-scale universe, but also the animals which inhabit it. As progeny of the universe, animals inherit certain cosmic blueprints. Perhaps it is only fitting that many analogues to the cosmic patterns could be found here on Earth on the backs of insects, in animal markings, even in human made monuments. If we could create a zoo of universes, each with a different topology, we might replicate all the animal markings from zebra stripes to leopard spots.

[1] A. M. Turing, Philos. Trans. R. Soc. London **B237**, 37 (1952).
[2] J. D. Murray, *Mathematical Biology* (Springer-Verlag, New York, 1989).
[3] D. G. Christopherson, Q. J. Math. (Oxford Ser.) **11**, 63 (1940).
[4] J. Levin, J. D. Barrow, E. F. Bunn, and J. Silk, Phys. Rev. Lett. **79**, 974 (1997).
[5] J. Levin, E. Scannapieco, and J. Silk, Class. Quantum Grav. **15**, 2689 (1998).
[6] J. Levin, E. Scannapieco, and J. Silk, Phys. Rev. D **58**, 103516 (1998).
[7] N. L. Balazs and A. Voros, Phys. Rep. **143**, 109 (1986).
[8] N. J. Cornish, D. Spergel, and G. Starkman, Class. Quantum Grav. **15**, 2657 (1998); Phys. Rev. D **57**, 5982 (1998).
[9] J. R. Bond, D. Pogosyan, and T. Souradeep, astro-ph/9702212 (1997); astro-ph/9804041 (1998).
[10] M. Lachieze-Rey and J. P. Luminet, Phys. Rep. **254**, 135 (1995).
[11] R. Lehoucq, M. Lachieze-Rey, and J. P. Luminet, ''Cosmic Crystallography,'' gr-qc/9604050.
[12] P. Ferreira and J. Magueijo, Phys. Rev. D **56**, 4578 (1997).
[13] B. F. Roukema and V. Blanloeil, Class. Quantum Grav. **15**, 2645 (1998).
[14] D. D. Sokolov and V. F. Shvartsman, Sov. Phys. JETP **39**, 196 (1975); G. Paal, Acta Phys. Acad. Sci. Hung. **30**, 51 (1971); J. R. Gott, Mon. Not. R. Astron. Soc. **193**, 153 (1980); I. Yu. Sokolov, JETP Lett. **57**, 617 (1993).
[15] D. Stevens, D. Scott, and J. Silk, Phys. Rev. Lett. **71**, 20 (1993).
[16] A. de Oliveira-Costa and G. F. Smoot, Astrophys. J. **448**, 477 (1995).
[17] J. Levin, E. Scannapieco, and J. Silk, ''Temperature correlations in a finite universe.''
[18] J. A. Wolf, *Spaces of Constant Curvature* (Publish or Perish, Wilmington, Delaware, 1967).
[19] U. Seljack and M. Zaldarriaga, Astrophys. J. **469**, 437 (1996).
[20] J. Weeks, Class. Quantum Grav. (to be published), astro-ph/9802012.
[21] P. F. Muciaccia, P. Natoli, and N. Vittorio, Astrophys. J. Lett. **488**, L63 (1997).
[22] M. C. Gutzwiller, J. Math. Phys. **11**, 1791 (1970); M. C. Gutzwiller, J. Math. Phys. , 343 (1971).
[23] W. P. Thurston, Bull. Am. Math. Soc. **6**, 357 (1982); W. P. Thurston and J. R. Weeks, Sci. Am. 94 (1984); W. P. Thurston, in Three-dimensional Geometry and Topology, edited by Silvio Levy (Princeton University Press, Princeton, NJ, 1997).
[24] L. A. Best, Can. J. Math. **23**, 451 (1971).
[25] J. R. Weeks, Ph.D. thesis, Princeton University, 1985.
[26] J. D. Barrow and J. Levin, Phys. Lett. A **233**, 169 (1997).
[27] G. D. Mostow, *Ann. Ath. Studies* (Princeton University Press, Princeton, 1973), Vol. 78; G. Prasad, Invent. Math. **21**, 255 (1973).
[28] J. Weeks, computer software *SnapPea* available at http://www.geom.umn.edu:80/software.
[29] H. V. Fagundes, Phys. Rev. Lett. **70**, 1579 (1992).
[30] H. V. Fagundes, Phys. Rev. Lett. **51**, 517 (1983); H. V. Fagundes, Astrophys. J. **338**, 618 (1989).
[31] G. T. Horowitz and D. Marolf, J. High Energy Phys. **9807**, 014 (1998).